JACS Au
AN OPEN ACCESS JOURNAL OF THE AMERICAN CHEMICAL SOCIETY

pubs.acs.org/jacsau

Article

Lanthanide-Based Peptide-Directed Visible/Near-Infrared Imaging and Inhibition of LMP1

Ho-Fai Chau, Yue Wu, Wan-Yiu Fok, Waygen Thor, William Chi-Shing Cho, Ping'an Ma, Jun Lin, Nai-Ki Mak, Jean-Claude G. Bünzli,* Lijun Jiang,* Nicholas J. Long,* Hong Lok Lung,* and Ka-Leung Wong*

Cite This: *JACS Au* 2021, 1, 1034–1043

Read Online

ACCESS | Metrics & More | Article Recommendations | Supporting Information

ABSTRACT: A lanthanide-based peptide-directed bioprobe **LnP19** (Ln = Eu or Yb) is designed as an impressive example of a small molecule-based dual-functional probe for the EBV oncoprotein LMP1. The peptide **P19** (Pra-KAhx-K-LDLALK-FWLY-K-IVMSDKW-K-RrRK) is designed to selectively bind to LMP1 by mimicking its TM1 region during oligomerization in lipid rafts while signal transduction is significantly suppressed. Immunofluorescence imaging and Western blotting results reveal that **P19** can effectively inactivate the oncogenic cellular pathway nuclear factor κB (NF-κB) and contribute to a selective cytotoxic effect on LMP1-positive cells. By conjugation with cyclen-based europium(III) and ytterbium(III) complexes, **EuP19** and **YbP19** were constructed to offer visible and near-infrared LMP1-targeted imaging and cancer monitoring. In addition to the ability to target and inhibit LMP1 and to selective inhibit LMP1-positive cells, selective growth inhibition toward the LMP1-positive tumor by **LnP19** is also demonstrated.

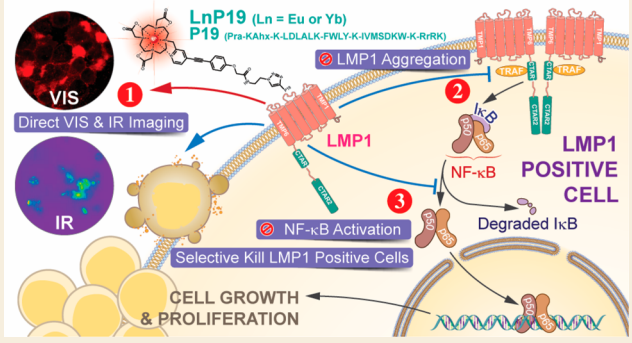

KEYWORDS: *LMP1-targeted imaging, EBV, EBV-related cancer, lanthanide(III) luminescence, theranostic agent*

INTRODUCTION

The Epstein–Barr virus (EBV) belongs to the gamma herpesvirus family, which infects more than 90% of the population worldwide.[1,2] Despite the widespread condition of EBV, a latent infection is developed in most cases. EBV tends to infect the B lymphocyte in an immunocompetent host, persist in the memory B cell pool, and the host remains asymptomatic with a life-long latent infection.[3] During a latent infection, only a handful of EBV latent genes are expressed. Latent membrane protein 1 (LMP1) is one of those viral gene products;[3] it is the major transforming protein of EBV and is critical for EBV-induced B-cell transformation *in vitro*.[6−8] LMP1 is also important in tumor cell proliferation, immortalization, and angiogenesis.[3−5] The oncogenic functions of LMP1 have been implicated in a variety of EBV-related cancers including Hodgkin's disease, non-Hodgkin lymphoma, nasopharyngeal carcinoma (NPC), and gastric cancer.[5] Taken together with its localization in the cell membrane, LMP1 is considered as an attractive therapeutic target in EBV-associated malignancies.

LMP1 is an integral membrane protein which has the molecular weight of 66 kDa. It contains three structural parts: a short 24 amino acid residue cytoplasmic N-terminus, six transmembrane domains (TM1-6) with five short reverse turns in between, and a long 200 amino acid residue cytoplasmic C-terminus.[4] It functions by mimicking the cell surface receptor CD40 to recruit tumor necrosis factor receptor associated signaling proteins in a ligand-independent manner.[9,10] This activates several cellular pathways including nuclear factor κB (NF-κB), mitogen-activated protein kinase, and phosphatidylinositol 3-kinase pathways.[11−13] Induction of transcription of multiple target genes will follow once these pathways are activated, leading to cell proliferation, invasion, and cell cycle progression.[14,15] While the cytosolic C-terminus portion of LMP1 is responsible for intracellular signal transduction which causes nuclear translocation of transcription factors, the transmembrane (TM) domains play a crucial role in signaling initiation at the cell membrane. The TM domains of LMP1 facilitate its aggregation and oligomerization in the lipid raft, causing LMP1 to be constitutively active for cellular signaling.[16] The TM1-2 domains contain the lipid raft targeting signals and thus are critical to cluster the LMP1 monomers via

Received: April 28, 2021
Published: June 20, 2021

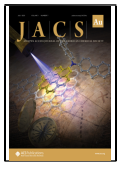

https://doi.org/10.1021/jacsau.1c00187
JACS Au 2021, 1, 1034–1043

association with the lipid raft.[17,18] These domains are also essential to mediate intermolecular interaction among the LMP1 monomers, which contributes in a large proportion of LMP1-mediated NF-κB activation, whereas other TMs do not have any role in signaling transduction.[17,19] Mutation in the TM1 domain of LMP1 resulted in reduction in protein stability and lipid raft aggregation.[20,21] Within TM1, its amino acid residue $FWLY_{38-41}$ was shown to play a crucial role in NF-κB activation, as the activation pathway was impaired upon $FWLY_{38-41}$ mutation, the intermolecular interaction between the TM domains was abrogated, and the association between the lipid raft and other signaling proteins was also weakened.[19]

Based on the critical role of $FWLY_{38-41}$ in the signaling pathway regulation, the peptide **P19** (Pra-KAhx-K-LDLALK-FWLY-K-IVMSDKW-K-RrRK) is designed to mimic the key amino acid residues in the TM1 region of LMP1. Pra (propargylcine) is included into the peptide to enable the conjugation of the peptide to the azide group in lanthanide(III) complexes. The incorporation of FWLY into the peptide can mimic the intermolecular interaction portion of LMP1TM1-2 and LMP1TM3-4, so as to disrupt the oligomerization among the LMP1 monomers in the lipid raft while inactivating the NF-κB signal transduction (Figure 1). An extended conformation of FWLY was adopted to facilitate the α-helix conformation which may have a role in biological functions of LMP1. Besides, lysine and aspartic acid were added to or replaced with some amino acids in the peptide to increase the solubility of the peptide. In the study, a control peptide, **P19C**, was also synthesized by replacing the FWLY residues with AAAA, which can help to demonstrate the functional significance of the FWLY motif. With the use of molecular docking, FWLY in **P19** is suggested to interact with the TM3-4 region of LMP1 with an estimated binding energy of −220 kcal/mol, while the residues AAAA, failing to show an α-helix structure, of **P19C** interact with the TM1-2 region which is considered unable to interrupt the intermolecular oligomerization of LMP1 (Figure S1). Furthermore, we would also like to determine if **P19** can be used for the direct visualization of LMP1.

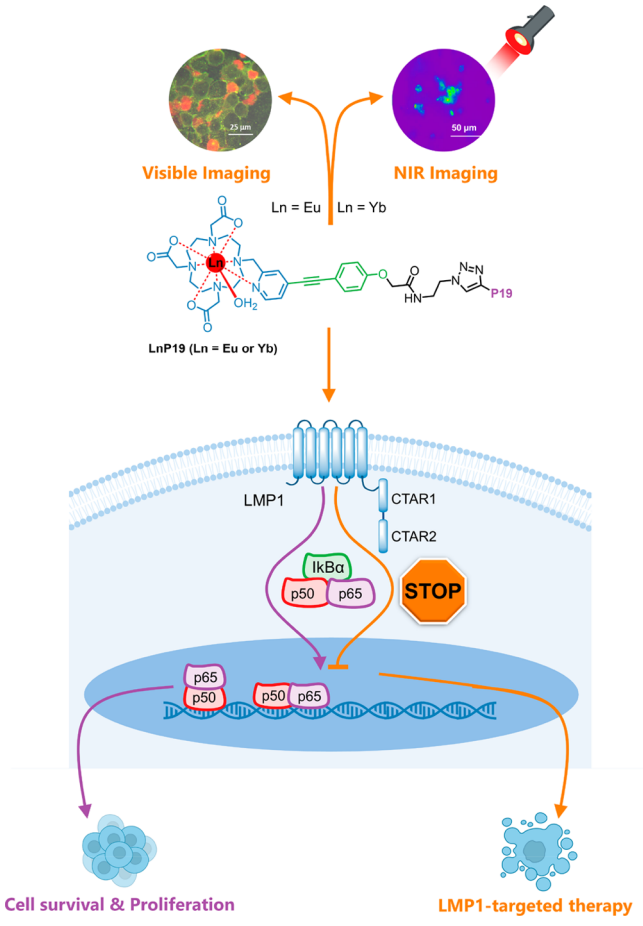

Figure 1. Schematic diagram of the visible and NIR imaging and the NF-κB inhibition capability of **EuP19** and **YbP19** on LMP1-positive cells (orange line, with the addition of our probe **LnP19**; violet line, without **LnP19**). Created with BioRender.com.

Immunofluorescence is an assay that relies on the use of antibodies labeled with fluorescent dyes to visualize cellular antigens such as proteins, which can be used for LMP1 imaging. However, the fixation procedure results in cell death and, hence, cannot provide real-time information in live cells. In addition, this assay is generally highly costly and has little flexibility. Luminescence of lanthanide(III) ions offers remarkable advantages for biological optical imaging. Sharp emission bands, large ligand-induced Stokes' shifts, and long luminescence lifetimes (μs to ms range) can benefit the signal-to-noise ratio enhancement of images by abolishing the interference due to the short-lived autofluorescence. A number of anticancer lanthanide(III)-based nanocargoes have been developed for targeting various specific proteins by peptides.[23−25] However, large size agents, including the above-mentioned nanosystems, have the potential risk of interfering with the biological systems.[22] Small-molecule probes offer many benefits, including minimal perturbation to the native function of the target. A methodological approach to construct molecular ytterbium(III) and neodymium(III) complexes conjugated with a targeting peptide as NIR imaging agents has been recently described.[22] The aim of the present study is therefore to develop lanthanide(III)-based peptide-directed small molecules for specific vis/NIR imaging and inhibition via targeting the oncoprotein LMP1. To the best of our knowledge, lanthanide-based LMP1-targeting agents with a direct imaging function have not been reported. In this work, the inhibitory effects on tumor growth and the NF-κB pathway and the fluorescent properties of our anti-LMP1 compounds on LMP1-positive cell lines are investigated and directly visualized by **EuP19** and **YbP19**.

RESULTS AND DISCUSSION

Synthesis and Photophysical Properties of LnP19

To synthesize the lanthanide(III)-based luminescent LMP1-targetting probes, a copper(I)-catalyzed alkyne−azide cycloaddition (CuAAC)[26] was conducted to incorporate alkyne-containing **P19** (there is an alkyne on the side chain of the amino acid residue Pra) into stable, emissive, and azide-containing cyclen-based europium(III) and ytterbium(III) complexes that were used in our previous studies;[27−30] the resulting conjugates **EuP19** and **YbP19** (Figure 2a), respectively, can simultaneously function as LMP1 imaging probes as well as therapeutic agents for EBV-associated cancer treatment. The synthetic route toward **LnP19** is shown in Figure S8. The intermediates are well-characterized by ^{1}H NMR and ^{13}C NMR spectrometry (Figures S9−24), and the final peptide conjugates are purified via preparative-HPLC,

https://doi.org/10.1021/jacsau.1c00187
JACS Au 2021, 1, 1034−1043

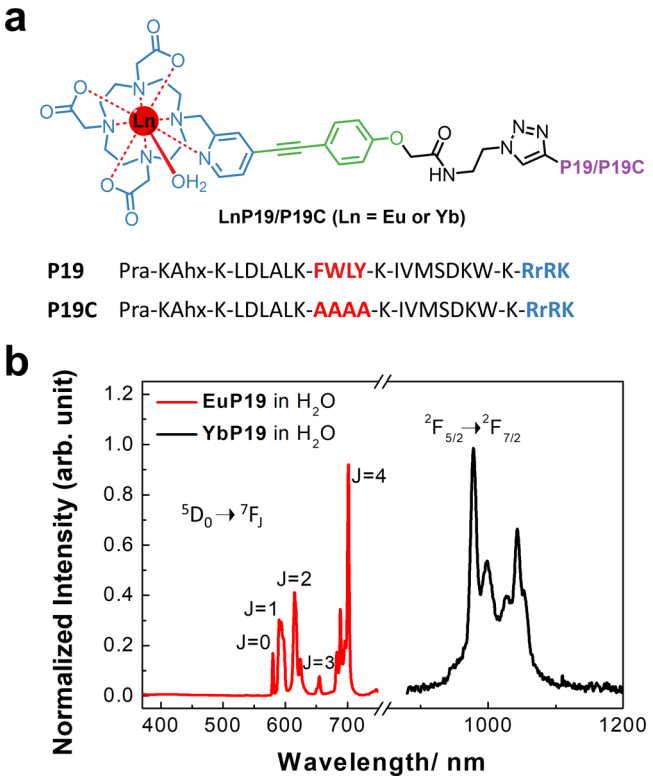

Figure 2. (a) Structures of **EuP19** and **YbP19** and sequences of **P19** and **P19C**. (b) Emission spectra of **EuP19** and **YbP19** (10 μM, λ_{ex} = 330 nm).

with the final characterization by analytical HPLC and HRMS spectrometry (Figures S25−32). Emissions in visible and near-infrared regions of **EuP19** and **YbP19** are illustrated in Figure 2b; no obvious emission from the ligand and/or protein is observed. The absorption and excitation spectra are included in Figure S2. The emission quantum yields of **EuP19** and **YbP19** are 8.3 ± 0.8% and 0.05 ± 0.005%, respectively. The lifetimes of **EuP19** in H_2O and D_2O were measured to calculate a *q*-value equal to 1.05 coordinated water molecules (Table S1).

Selective Cytotoxicity toward Highly LMP1-Positive Cell Lines

To study the effects of our designed probes on cell survival, the MTT cytotoxicity assay was carried out in several highly LMP1-positive (LCL3, AFB1, AG876), weakly LMP1-positive (C666-1), and LMP1-negative cell lines (HeLa, MRC5), as shown in Figure S3. Table 1 summarizes the cytotoxicity of **P19C**, **P19**, **EuP19**, and **YbP19** in these cell lines, shown as LC_{50} values. The data reveal that **P19**, **EuP19**, and **YbP19** possess selective cytotoxicity toward highly LMP1-positive cells as their LC_{50} are 10.3−36.9 μM (Table 1). On the other hand, their cytotoxicities on weakly LMP1-positive or LMP1-negative cells are relatively low, particularly in C666-1 cells, where the LC_{50} is determined to be ≥100 μM. **P19C** with the control peptide is not cytotoxic to any of the selected cell lines, because the LC_{50} values are over 200 μM for all selected cell lines. By comparing the cytotoxicity results against **P19C**, it can be seen that **P19**, **EuP19**, and **YbP19** have potential in their therapeutic effects for diseases associated with LMP1.

Co-localization of EuP19 and LMP1 in LMP1-Expressive Cell Lines

In order to investigate the subcellular localization of the LMP1-targeting peptide **P19**, the red-emissive **EuP19** was used to determine its application in imaging LMP1. This immunoluminescence imaging experiment of LMP1-over-expressing cells simultaneously allowed us to evaluate the targeting ability of **EuP19** for LMP1. First, LMP1-over-expressing cells were incubated with 10 μM of **EuP19** for different durations. The subcellular localization of LMP1 expression was detected by immunoluminescence imaging. As shown in Figure 3a, overlapping of the LMP1 (in green) signal with the red **EuP19** signal was observed in LCL3 and AFB1 cells upon a long incubation time (12 h) (Pearson's coefficient (ranging from −1 to 1) for **EuP19** in LCL3, 0.341, and in AFB1, 0.384).[31] **EuP19** is barely detectable in LCL3 cells after 2 h of incubation (Figure S4). **EuP19** was found to colocalize with the LMP1 protein at the LCL3 cell membrane, as reflected by overlapping yellow signals. The signals from **EuP19** in C666-1 cells were much weaker, but they were also colocalized with the LMP1 expression as observed in the C666-1 images with enhanced brightness (Pearson's coefficient for **EuP19** in C666-1 enhanced, 0.216).[31] However, the absence of a signal in both **EuP19** and LMP1 was observed in the LMP1-negative HeLa cells (Figure 3a). These imaging results suggest that **EuP19** can target the LMP1 protein on cell membranes and may interfere with the downstream signaling transduction pathway(s). In addition, z stacks scanning imaging has been conducted for clear identification of **EuP19** colocalization with LMP1 in LCL3 cells. 2D immunoluminescence images of the maximum intensity (Figure 3b) generated from the z stacks of LCL3 after treatment of **EuP19** for 12 h (Figure 3c) demonstrate obvious overlapping of the **EuP19** and LMP1 signals (Pearson's coefficient: 0.305).[31] In the pursuit of betterment of biological live imaging, the red emissive signal of **EuP19** in LCL3 was captured under two-photon excitation in the infrared range λ_{ex}: 740 nm (Figure 3d).

In order to detect the interaction between **EuP19** and LMP1, the LCL3 total cell lysate was fractionated by a protein gel and transferred to a PVDF membrane and then incubated with **EuP19**, and the light colored bands were detected by the luminescence signal of **EuP19** (Figure 3e, left). A similar pattern of bands could be observed using an LMP1 specific antibody by a parallel Western blot in using the same LCL3 cell lysate (Figure 3e, right). This implies notable binding

Table 1. Summary of the LC_{50} Values of P19C, P19, EuP19, and YbP19 in Different Cell Lines

LC_{50}[a] (μM)	LCL3	AFB1	AG876	C666-1	HeLa	MRC5
P19C	>200	>200	>200	>200	>200	>200
P19	14.8 ± 0.76	13.6 ± 2.33	26.4 ± 3.06	71.1 ± 4.58	94.0 ± 4.15	108 ± 0.93
EuP19	12.4 ± 2.07	19.1 ± 3.60	38.7 ± 5.63	66.7 ± 4.48	123 ± 5.51	111 ± 2.52
YbP19	15.4 ± 1.32	16.2 ± 2.76	36.5 ± 4.31	78.6 ± 1.22	127 ± 2.88	98.3 ± 3.10

[a]Data are expressed as mean ± standard deviation.

https://doi.org/10.1021/jacsau.1c00187
JACS Au 2021, 1, 1034−1043

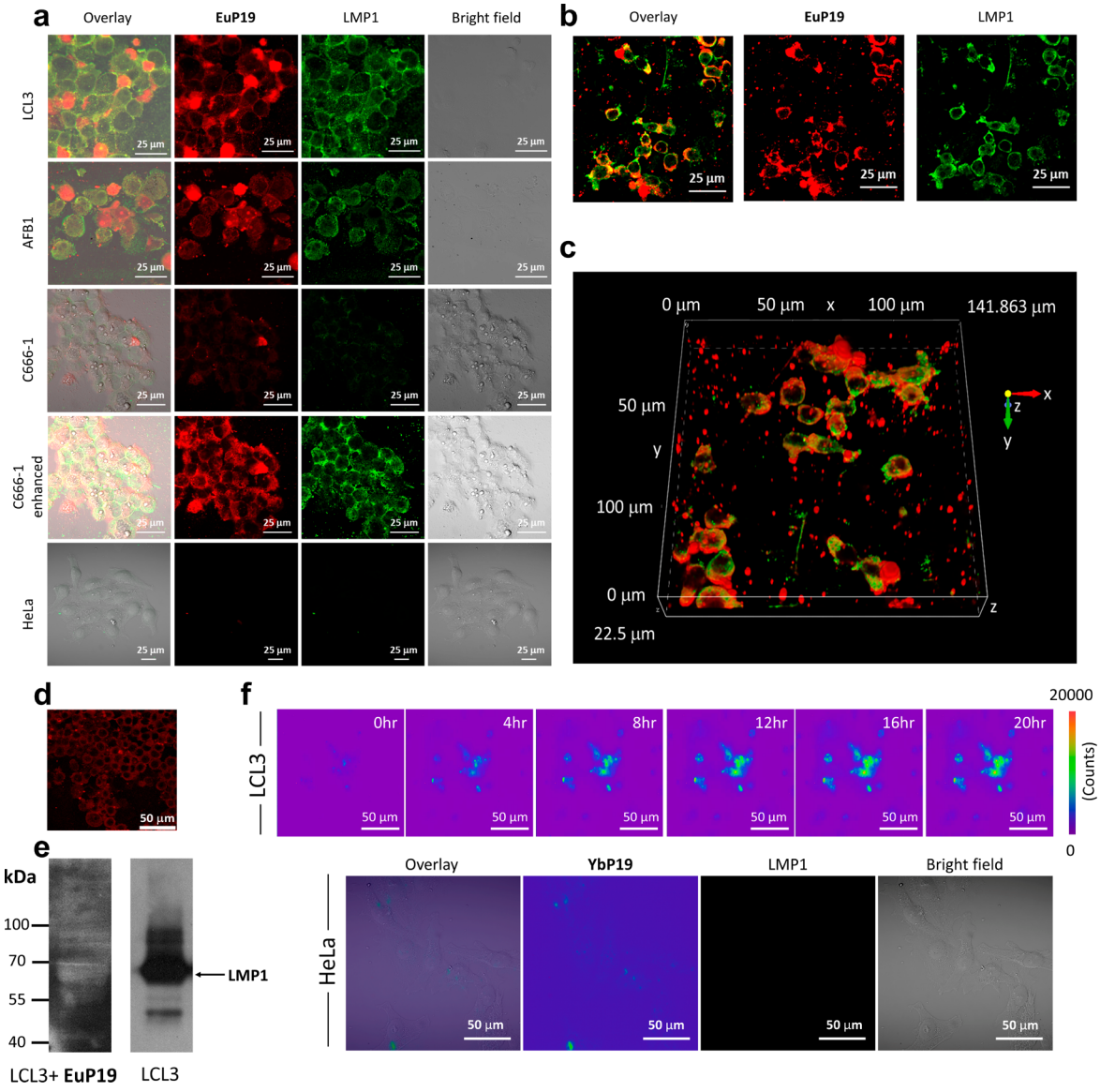

Figure 3. (a) Immunoluminescence imaging of the LMP1 protein and **EuP19** in LCL3, AFB1, C666-1, and HeLa cells after 12 h of incubation. (Enhanced brightness of luminescence signals in C666-1 are shown underneath the original images for the C666-1 cells; [**EuP19**] = 10 μM; λ_{ex} = 370 nm; λ_{ex} of LMP1 staining dye = 491 nm; scale bar, 25 μm). (b) Immunoluminescence images of LMP1 and **EuP19** in LCL3 in the *xy* plane with the maximum signal intensity generated from the z stack scanning (scale bar, 25 μm). (c) Z stacks of 2D images of LMP1 and **EuP19** in LCL3 cells ([**EuP19**] = 10 μM; λ_{ex} = 370 nm; incubation time = 12 h; λ_{ex} of LMP1 staining dye = 491 nm). (d) Imaging of **EuP19** in LCL3 by multiphoton microscopy ([**EuP19**] = 10 μM; λ_{ex} = 740 nm; incubation time = 12 h; scale bar, 50 μm). (e) Western blot detection of LMP1 (right) and luminescence signal of **EuP19** (left). (f) NIR live images of **YbP19** in LCL3 cells after different incubation times up 20 h and NIR images of **YbP19** in HeLa after 12 h incubation ([**YbP19**] = 10 μM; λ_{ex} = 370 nm; scale bar, 50 μm).

between **EuP19** and LMP1 was detected in Figure 3e. Thanks to the near-infrared (NIR) emission from ytterbium(III) in **YbP19**, NIR live imaging of LMP1 is observed in LCL3 cells with continuous enhancement in the NIR signal of LMP1 within 20 h of incubation time (Figure 3f), while nearly no NIR signal can be obtained in the LMP1-negative HeLa cells (Figure 3f). The effective LMP1-targeting and the vis/NIR imaging ability makes **EuP19** and **YbP19** the first lanthanide-based bioprobes for direct LMP1 visualization and monitoring of LMP1-associated cancers.

Activity of NF-κB Is Significantly Suppressed by P19, EuP19, and YbP19

We then investigate the inhibitory effects of our anti-LMP1 conjugates on the NF-κB pathway, which is one of the major pathways that EBV has hijacked for promoting cell growth and proliferation in EBV-associated tumors. Since NF-κB is typically activated by the canonical pathway which involves the nuclear translocation of the heterodimer of p50 and p65,[32] immunofluorescence imaging of NF-κB p65 was then performed. Tumor necrosis factor alpha (TNFα) was added to these tumor cells, so as to activate the NF-κB pathway. As shown in Figure 4a, there was significant suppression of the green fluorescence p65 signal in LCL3 in the presence of **P19**, **EuP19**, and **YbP19**. However, no significant effect was observed with **P19C** and in the control group without any compound. Furthermore, when using the pTRE-EGFP reporter to detect the NF-κB activity, the results showed that the green fluorescent protein (GFP) signals decreased when

https://doi.org/10.1021/jacsau.1c00187
JACS Au 2021, 1, 1034−1043

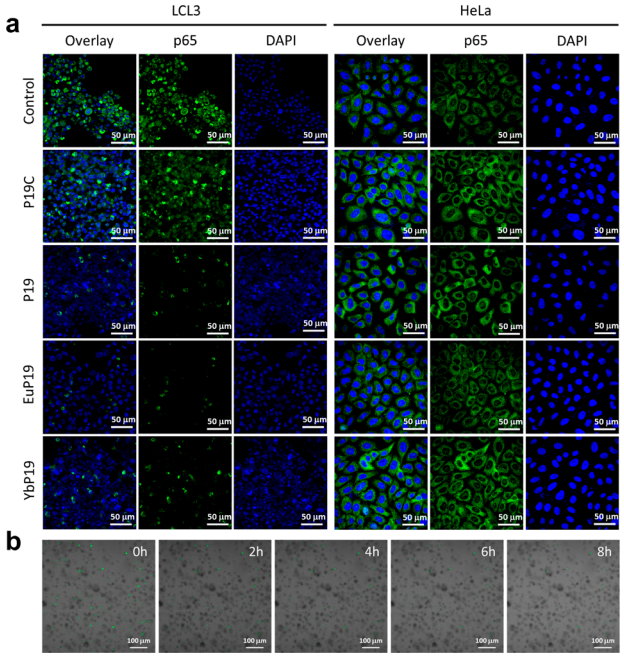

Figure 4. (a) Immunofluorescence imaging of NF-κB p65 in LCL3 and HeLa cell lines ([**P19**] = 10 μM, [**EuP19**] and [**YbP19**] = 10 μM, incubation time = 24 h; preincubation [TNFα] = 10 ng/mL, incubation time = 30 min; λ_{ex} of NF-κB staining dye = 491 nm; λ_{ex} of DAPI = 405 nm; scale bar, 50 μm). The green fluorescence is from p65 while the blue fluorescence is from DAPI, a nucleus dye serving as the control. (b) Confocal live imaging of the NF-κB reporter LCL3 cells with 10 μM **EuP19** incubation (λ_{ex} = 491 nm; scale bar, 100 μm).

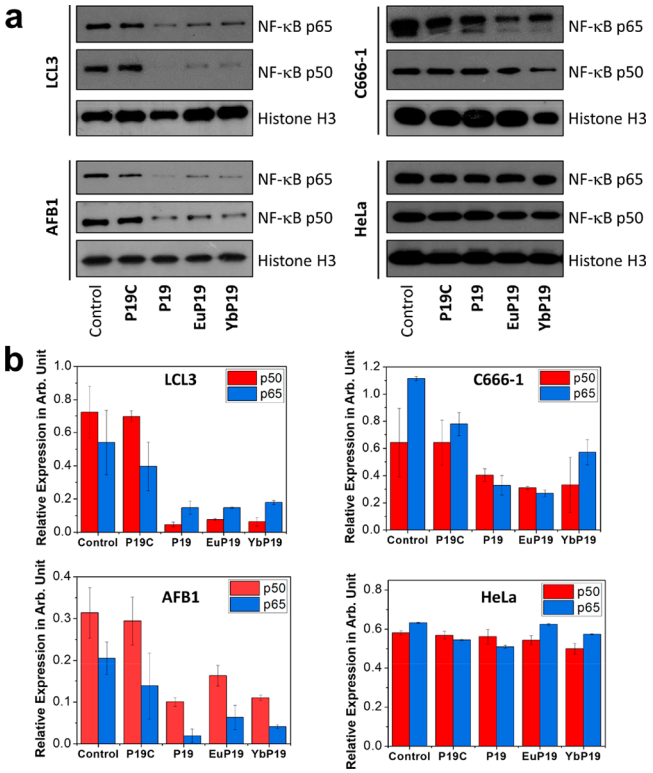

Figure 5. (a) Western blot results and (b) the bar charts of NF-kB p65 and p50 in LCL3, AFB1, C666-1, and HeLa after the incubation with 20 μM **P19**, **EuP19**, and **YbP19** for 30 min (preincubation with TNFα, 10 ng/mL for 30 min, histone H3 serves as the loading control).

LCL3 was treated with **P19** for 6 h (Figure 4b), suggesting that **P19** can greatly suppress both the expression of NF-κB p65 and its activity. In contrast, strong green fluorescence was observed in LMP1-negative HeLa cells (Figure 4a) and weak LMP1-expressing C666-1 cells (Figure S5), showing that **P19** did not exhibit any effect on the NF-κB pathway in cell lines with low levels of LMP1 expression. The results of using **EuP19** and **YbP19** were similar to those of **P19**, demonstrating the great potential of these two conjugates as both LMP1-specific NF-κB inhibitors and imaging agents.

Western blot analysis was also carried out to validate the above imaging results for the components in the NF-κB pathway. The LMP1-overexpressing LCL3 and AFB1 cell lines were used for this analysis. The cells were pretreated with TNFα (10 ng/mL; incubated with the cells for 30 min for activation of the NF-κB pathway before the addition of **P19C**, **P19**, **EuP19**, and **YbP19**). After 24 h of incubation, the nuclear extracts were separated for each treatment, and the expression of NF-κB p65 and p50 was detected by Western blot analysis. Results showed that the nuclear p65 and p50 expressions in LCL3 and AFB1 were significantly weakened after being treated with **P19**, **EuP19**, and **YbP19**, compared with the control (Figure 5). Furthermore, there was no obvious change in the expression of these two proteins when **P19C** was used, whereas the changes in the expression of p65 and p50 were relatively minor in C666-1 and HeLa cells (Figure 5). Western blots of individual replicates for NF-κB p65 and p50 in different cell lines are illustrated in Figure S6. Altogether, the Western blot results are coherent with the immunostaining of NF-κB p65 evidenced in the imaging experiments, indicating that **P19**, **EuP19**, and **YbP19** can suppress the expression and activity of NF-κB p65 and p50 in cell lines with high levels of LMP1. The reduction in NF-κB activity can contribute to the cytotoxicity of the three compounds toward LMP1-overexpressing cells.

Significant Tumor Growth Inhibition in Xenograft Models by EuP19

The LCL3-derived xenograft mouse model was used to examine the inhibitory effect of **EuP19** *in vivo*. **EuP19**, **P19C**, and PBS were administered to three groups of LCL3 xenografts by intratumor injection twice per week under the dosage of 25 μg/tumor. Representative tumor pictures were taken after the treatment. The results illustrate an obvious decrease in the tumor sizes of the **EuP19** treatment group (Figure 6a). On day 16, the average tumor volume of this group was significantly lower than those of the two control groups (i.e., PBS and **P19C**) (Figure 6b). This outcome is in agreement with the *in vitro* cytotoxicity results, showing that **EuP19** can effectively inhibit both *in vitro* and *in vivo* growth of LMP1-overexpressing tumor cells. In addition, cell necrosis can be observed in tumor nodules in the LCL3 xenografts treated with **EuP19** (Figure 6c). It may associate with the cytotoxic activity of **EuP19**. However, tightly packed cancer cells can be found in the control tumors (Figure 6c). Besides, there is no significant effect on the mice body weights after treatment with **EuP19** when compared with the control groups (Figure S5), indicating this dosage of **EuP19** is safe for the animal. Therefore, **EuP19** is considered as a safe and specific theranostic agent to treat LMP1-positive tumors.

The FWLY amino acid residues were included in **P19**, which functions as a decoy to mimic the TM1-2 region of LMP1.

https://doi.org/10.1021/jacsau.1c00187
JACS Au 2021, 1, 1034−1043

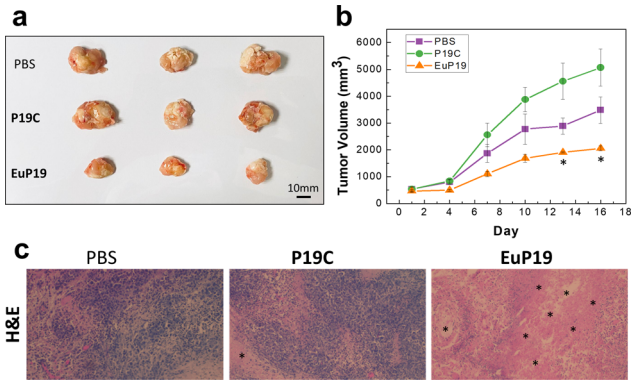

Figure 6. (a) Images of the LCL3-xenograft model in different treatment groups. (b) Change in average LCL3 tumor volume of the xenograft model under different treatments; data are expressed as mean ± SEM. * refers to $P < 0.1$ vs PBS control, a statistically significant difference. (c) Representative images of the center region of PBS control, **P19C**, and **EuP19** (acellular regions indicated by *) treated tumors formed by LCL3 cells.

That design can contribute to the binding with LMP1. The self-association of the LMP1 monomer will be disrupted when the LMP1 TM3-4 regions in one monomer bind with **P19** via the FWLY residues, instead of binding with the TM1-2 regions of another LMP1 monomer. The downstream signal transduction, including the canonical NF-κB pathway, can then no longer be stimulated since **P19** is lacking the functional LMP1 C-terminus. Inhibition of the oncogenic NF-κB pathway can significantly inhibit cell proliferation in LMP1-overexpressing cells, thus leading to high cytotoxicity. We have made use of emissive europium(III) or ytterbium(III) chelates conjugated with the LMP1-specific peptide **P19** to test for their imaging capabilities in various LMP1-expressive and nonexpressive cells. The imaging results demonstrate for the first time the feasibility of direct and real-time visualization of LMP1 in EBV-infected cells. Our imaging results confirmed that **EuP19** was colocalized with expressed LMP1, which was primarily present at the cellular membrane of the three LMP1-positive cell lines (LCL3, AFB1, C666-1).

However, differences were observed between the various cells. For instance, the red emission of **EuP19** generated from C666-1 was weak, contrary to what was observed with LCL3 and AFB1, which clearly reflects the weak membrane LMP1 expression of C666-1 and confirms the localization of the luminescent bioprobe on the membrane. Therefore, not only the subcellular localization but also the signal intensity of **EuP19** correlate well with the LMP1 expression. The weak LMP1 expression seems to make C666-1 cells unresponsive to our compounds, as seen in other LMP1-positive cell lines. In C666-1 cells, a frameshift mutation was identified in CYLD, a negative regulator of the NF-κB pathway, resulting in complete loss of the CYLD protein expression in this cell model.[33] It is likely that this NF-κB pathway aberration has already replaced the role of LMP1 in activating the NF-κB pathway for tumor growth. That could explain why this particular cell line did not respond well to our anti-LMP1 agents and also why only a portion of NPC tumors are LMP1-positive (~25 to 40%).[32] The absence of LMP1 expression has the advantage for tumor cells to escape from immune cell recognition. This cohort of NPC patients with positive LMP1 expression will be the target for our new anti-LMP1 drugs and imaging agents.

While **P19** possesses great potential in therapeutic intervention due to its selective growth inhibition for LMP1-overexpressing cells, **EuP19** and **YbP19** with similar cell cytotoxicities offer the additional advantage of the visualization of LMP1, which will be beneficial for monitoring the treatment efficacy. **EuP19** was also found to inhibit tumor growth on the LMP1-overexpressing LCL3 xenograft model, suggesting that the therapeutic properties of **P19** are retained after appending onto the europium(III) complex.

By traditional chromogenic immunohistochemical (IHC) methods, the detection of LMP1 in the NPC cases varies between 20−60%.[34,35] The low detection rates of LMP1 in NPC are probably due to the low levels of LMP1 expression in some NPC tissues, which cannot be detected by conventional IHC. Those low levels of LMP1 expression are sufficient to activate the NF-κB-mediated cell growth and survival.[36] Importantly, LMP1 protein is detected in almost all premalignant or preinvasive NPC tissues, suggesting the contribution of LMP1 during the early stage of NPC pathogenesis.[34,35] Our LMP1-specific therapeutic probes **EuP19** and **YbP19** demonstrated a high potential to provide a much more sensitive means of detection of the low LMP1 expression in NPC tissues which cannot be detected by conventional IHC. Moreover, our new LMP1 probes can also be used for early detection of NPC tumors with LMP1 expression.

CONCLUSION

Our study presents the first live visualization of LMP1 in EBV-positive tumor cells by the tailored LMP1-specific therapeutic probes **EuP19** and **YbP19**. On the other hand, LMP1-positive tumors are known to be more progressive than LMP1-negative tumors and prone to lymph node metastasis. They are associated with poor overall survival, and LMP1 is also a strong risk factor for poor prognosis in NPC.[37−41] Our LMP1 probes exhibit high cytotoxicity toward LMP1-expressing cells by suppressing the NF-κB pathway, and these probes can contribute to the therapeutic potential against advanced NPC with poor survival under conventional therapies.

EXPERIMENTAL SECTION

Synthesis

The synthetic route is outlined in Figure S8. Briefly, the azide-containing antenna (compound **S7**) was constructed via multistep reactions which include two Sonogashira couplings and direct amination of methyl ester with an azide-containing linker (compound **S6**). The antenna was then installed onto the cyclen core (tBu-DO_3A, **S8**), and the corresponding lanthanide complexes (**Ln-N_3**) were obtained after deprotection of *tert*-butyl ester and coordination with lanthanide ion. Finally, the CuAAC reaction was carried out between the azide on the lanthanide(III) complexes and the alkyne on the peptide (from the side chain of Pra, propargylglycine) to give the desired lanthanide−peptide conjugates.

Synthesis of (4-((Trimethylsilyl)ethynyl)pyridin-2-yl)methanol (S2)

Under an inert atmosphere, a mixture of (4-bromopyridin-2-yl)methanol (**S1**, 10 mmol), ethynyltrimethylsilane (12 mmol), $Pd(PPh_3)_4$ (0.1 mmol), CuI (0.05 mmol), and DIPEA (20 mmol) in THF (50 mL) was heated at 45 °C overnight. Upon completion, the reaction mixture was filtered, and the filtrate was concentrated and purified by column chromatograph on silica gel (eluent: hexane/EA, v/v, 3/1 to 1/1), to give the desired product. White solid. Yield 71%. ^{1}H NMR (400 MHz, chloroform-*d*) δ 8.49−8.44 (m, 1H), 7.33−7.29 (m, 1H), 7.20 (dd, J = 5.2, 1.5 Hz, 1H), 4.72 (s, 2H), 4.13−4.06 (m,

https://doi.org/10.1021/jacsau.1c00187
JACS Au 2021, 1, 1034−1043

1H), 0.25 (s, 9H); ^{13}C NMR (101 MHz, chloroform-*d*) δ 159.42, 148.43, 131.94, 124.46, 122.79, 101.91, 100.14, 64.05, −0.34.

Synthesis of (4-Ethynylpyridin-2-yl)methanol (S3)

To a solution of (4-((trimethylsilyl)ethynyl)pyridin-2-yl)methanol (**S2**, 10 mmol) in MeOH (50 mL), K_2CO_3 (20 mmol) was added in one portion at 0 °C. The mixture was then stirred at r.t. for 30 min. The reaction was monitored by TLC (eluent: hexane/EA, v/v, 1/1). Upon completion, the solvent was evaporated and then extracted with DCM/water. The organic layer was combined, concentrated, and then purified by column chromatography on silica gel (eluent: hexane/EA, v/v, 3/1 to 1/1), to give the desired product. White solid. Yield 87%. ^{1}H NMR (400 MHz, chloroform-*d*) δ 8.52 (dd, J = 5.1, 0.9 Hz, 1H), 7.34 (dd, J = 1.6, 0.9 Hz, 1H), 7.26 (dd, J = 5.3, 1.4 Hz, 1H), 4.75 (d, J = 3.6 Hz, 2H), 3.78 (d, J = 4.7 Hz, 1H), 3.29 (s, 1H); ^{13}C NMR (101 MHz, chloroform-*d*) δ 159.79, 148.60, 131.12, 124.76, 123.11, 82.06, 82.02, 64.08.

Synthesis of Methyl 2-(4-Iodophenoxy)acetate (S4)

The suspension of 4-iodophenol (20 mmol), methyl 2-bromoacetate (22 mmol), and K_2CO_3 (44 mmol) in acetone (50 mL) was refluxed at 60 °C for 12 h. Upon completion, the solvent was vaporized and then extracted with DCM/water. The organic layer was combined, concentrated, and then purified by column chromatography on silica gel (eluent: hexane/EA, v/v, 20/1 to 10/1), to give the desired product. White solid. Yield 84%. ^{1}H NMR (400 MHz, chloroform-*d*) δ 7.65−7.50 (m, 2H), 6.74−6.62 (m, 2H), 4.60 (s, 2H), 3.80 (d, J = 0.8 Hz, 3H); ^{13}C NMR (101 MHz, chloroform-*d*) δ 169.01, 157.69, 138.42, 117.02, 84.18, 65.27, 52.37.

Synthesis of Methyl 2-(4-((2-(Hydroxymsethyl)pyridin-4-yl)ethynyl)phenoxy)-acetate (S5)

Under an inert atmosphere, a mixture of 2-(bromomethyl)-4-ethynylpyridine (**S3**, 5 mmol), methyl 2-(4-iodophenoxy)acetate (**S4**, 6 mmol), $Pd(PPh_3)_4$ (0.05 mmol), CuI (0.025 mmol), and DIPEA (10 mmol) in THF (30 mL) was heated at 45 °C overnight. Upon completion, the reaction mixture was filtered, concentrated, and extracted with DCM/water. The combined organic layer was washed with an EDTA solution, concentrated, and purified by column chromatography on silica gel (eluent: hexane/EA, v/v, 3/1 to 1/1), to give the desired product. White solid. Yield 76%. ^{1}H NMR (400 MHz, chloroform-*d*) δ 8.47 (d, J = 5.1 Hz, 1H), 7.46 (d, J = 8.4 Hz, 2H), 7.36 (s, 1H), 7.23 (d, J = 5.2 Hz, 1H), 6.88 (d, J = 8.4 Hz, 2H), 4.74 (s, 2H), 4.64 (s, 2H), 4.28 (s, 1H), 3.79 (s, 3H); ^{13}C NMR (101 MHz, chloroform-*d*) δ 168.92, 159.62, 158.41, 148.47, 133.59, 132.41, 124.07, 122.35, 115.29, 114.80, 93.97, 86.03, 65.13, 64.21, 52.42.

Synthesis of 2-Azidoethan-1-aminium chloride (S6)

The solution of 2-chloroethan-1-amine (20 mmol) and NaN_3 (40 mmol) in water (100 mL) was heated at 80 °C for 12 h. Upon completion, the pH of the solution was adjusted to 14 by 1 M NaOH. Then, the resultant mixture was extracted by DCM, and the combined organic fractions were dried with Na_2SO_4. The solution was filtered, the filtrate was mixed with an equal volume of water, then the pH was adjusted to 1 by 1 M HCl, and all the solvents were evaporated to give a white solid as a hydrochloride salt. Yield 65%. ^{1}H NMR (400 MHz, DMSO-d_6) δ 8.38 (s, 3H), 3.68−3.63 (m, 2H), 2.93 (h, J = 5.7 Hz, 2H); ^{13}C NMR (101 MHz, DMSO-d_6) δ 47.94, 37.84.

Synthesis of *N*-(2-Azidoethyl)-2-(4-((2-(hydroxymethyl)pyridin-4-yl)-ethynyl)phenoxy)acetamide (S7)

The solution of methyl-2-(4-((2-(hydroxymethyl)pyridin-4-yl)-ethynyl)phenoxy)acetate (**S5**, 5 mmol), 2-azidoethan-1-aminium chloride (**S6**, 15 mmol), and TEA (30 mmol) in 30 mL of THF/MeCN, v/v, 1/1 was heated at 60 °C for 2 d. The reaction was monitored by TLC (eluent: EA). Upon completion, the reaction mixture was concentrated and purified by column chromatography on silica gel (eluent: hexane/EA, v/v, 2/1 to 0/1). White solid. Yield 47%. ^{1}H NMR (400 MHz, chloroform-*d*) δ 8.51 (d, J = 5.2 Hz, 1H), 7.54−7.48 (m, 2H), 7.39−7.33 (m, 1H), 7.27−7.25 (m, 1H), 6.95−6.83 (m, 3H), 4.75 (s, 2H), 4.52 (s, 2H), 3.91 (s, 1H), 3.50 (s, 4H); ^{13}C NMR (101 MHz, chloroform-*d*) δ 168.03, 159.43, 157.63, 148.51, 133.76, 132.23, 124.10, 122.27, 115.85, 114.91, 93.62, 86.26, 67.23, 64.15, 50.73, 38.49.

Synthesis of Tri-*tert*-butyl 2,2′,2″-(1,4,7,10-Tetraazacyclododecane-1,4,7-triyl)-triacetate (S8, tBu-DO3A)

To a suspension of cyclen (29 mmol) and sodium acetate (96 mmol) in *N*,*N*-dimethylacetamide (DMA, 60 mL) at −18 °C (ice bath with saturated NH_4Cl) was added a solution of *t*-butyl bromoacetate (96 mmol) in DMA (20 mL) dropwise over a period of 30 min. The temperature was maintained at −18 °C during the addition. Then the reaction mixture was allowed to warm to r.t. After vigorous stirring for 24 h, the reaction mixture was poured into water (300 mL) to give a clear solution. Solid $KHCO_3$ (150 mmol) was added portionwise, and the product precipitated as a white solid. The precipitate was collected by filtration and dissolved in $CHCl_3$ (250 mL). The solution was washed with water (100 mL), dried (Na_2SO_4), filtered, and concentrated until only around 20−30 mL. Diethyl ether (250 mL) was added, and the product precipitated as a white fluffy solid. Yield 79%. ^{1}H NMR (400 MHz, chloroform-*d*) δ 10.21 (s, 1H), 3.33 (s, 4H), 3.24 (s, 2H), 3.03 (t, J = 4.9 Hz, 4H), 2.91−2.79 (m, 12H), 1.41 (s, 18H), 1.40 (s, 9H); ^{13}C NMR (101 MHz, chloroform-*d*) δ 170.54, 169.66, 81.76, 81.64, 58.21, 51.28, 49.15, 47.57, 28.23, 28.19.

Synthesis of Tri-*tert*-butyl 2,2′,2″-(10-((4-((4-(2-((2-Azidoethyl)amino)-2-oxoethoxy)-phenyl)ethynyl)pyridin-2-yl)-methyl)-1,4,7,10-tetraazacyclododecane-1,4,7-triyl)-triacetate (S9)

To a solution of *N*-(2-azidoethyl)-2-(4-((2-(hydroxymethyl)pyridin-4-yl)ethynyl)phenoxy)acetamide (**S7**, 4 mmol) and DIPEA (12 mmol) in DCM (15 mL), MsCl (6 mmol) in DCM (15 mL) was added dropwise. The resulting mixture was stirred at r.t. for 30 min. The reaction was monitored by TLC (eluent: EA). Upon completion, the reacting mixture was concentrated under vacuum. Then the resulting solid was redissolved in MeCN (20 mL), followed by adding K_2CO_3 (8 mmol) and tBu-DO_3A (**S8**, 3.6 mmol). The mixture was heated at 50 °C overnight. The reaction can be monitored by ESI-MS until the signal of **S8** is no longer detected. Upon completion, the reaction mixture was filtered, and the filtrate was evaporated followed by extraction with DCM/water. The organic layer was combined, concentrated, and then purified by column chromatography on silica gel (eluent: DCM/MeOH, v/v, 50/1 to 10/1) to give a white powder. Yield 68%. ^{1}H NMR (400 MHz, chloroform-*d*) δ 8.36 (d, J = 5.9 Hz, 1H), 8.14 (d, J = 5.1 Hz, 1H), 7.41−7.37 (m, 2H), 7.21 (s, 1H), 7.14 (dd, J = 5.1, 1.5 Hz, 1H), 6.97−6.93 (m, 2H), 4.60 (s, 2H), 3.48−3.44 (m, 4H), 3.38 (s, 2H), 3.05−2.15 (m, 22H), 1.42 (s, 9H), 1.34 (s, 18H); ^{13}C NMR (101 MHz, chloroform-*d*) δ 172.59, 168.43, 158.69, 158.53, 148.63, 133.53, 132.77, 125.04, 123.85, 115.21, 114.50, 95.04, 85.32, 82.12, 67.06, 58.62, 55.40, 53.50, 50.31, 50.25, 38.33, 27.94, 27.89.

General Synthetic Procedure for Ln-N_3

The solution of tri-*tert*-butyl 2,2′,2″-(10-((4-((4-(2-((2-azidoethyl)-amino)-2-oxoethoxy)phenyl)ethynyl)pyridin-2-yl)methyl)-1,4,7,10-tetraazacyclododecane-1,4,7-triyl)triacetate (**S9**, 0.05 mmol) in 2 mL of TFA/DCM, v/v, 1/1, was stirred for 16 h. Upon completion, the solvent was evaporated, and 0.5 mL of MeOH, 0.5 mL of deionized water, and 0.06 mmol of $EuCl_3 \cdot H_2O$ were added. The pH of the solution was adjusted to 7−8 by adding 1 M NaOH (aq) and stirred at r.t. for 12 h. The product was then purified by preparative-HPLC. *Eu*-N_3. Pale-yellow powder. Yield 48.5%. Analytical HPLC: retention time, 12.2 min; purity, 94.4%. MALDI-TOF HRMS: calcd for $[M - H_2O + H]^+$ 830.2128, found 830.2160. *Yb*-N_3. Pale-yellow powder. Yield 47.9%. Analytical HPLC: retention time, 12.9 min; purity,

https://doi.org/10.1021/jacsau.1c00187
JACS Au 2021, 1, 1034−1043

94.8%. MALDI-TOF HRMS: calcd for $[M - H_2O + H]^+$ 851.2305, found 851.2368.

General Synthetic Procedure of LnP19

Under an inert atmosphere, a mixture of **Ln-N_3** (0.02 mmol), **P19** (0.018 mmol), $Cu(CH_3CN)_4PF_6$ (0.02 mmol), TBTA (0.02 mmol), and DIPEA (0.1 mmol) was stirred at r.t. for 2−4 days; the final product was purified by preparative-HPLC. *EuP19.* Pale-yellow powder. Yield 34%. Purity 97.2%. Analytical HPLC: retention time, 29.4 min; purity, 96.7%. MALDI-TOF HRMS: calcd for $[M - H_2O + H]^+$ 4288.2600, found 4288.2564. *YbP19.* Pale-yellow powder. Yield 41%. Purity 96.7%. Analytical HPLC: retention time, 28.4 min; purity, 96.7%. MALDI-TOF HRMS: calcd for $[M - H_2O + H]^+$ 4309.2776, found 4309.2628.

Quantum Yield

The quantum yield of **EuP19** was measured using the method relative to the $[Eu(TTA)_3Phen]$ emission in DMF (λ_{ex} = 360 nm), while that of **YbP19** was measured relative to the NIR emission of $[Yb(TTA)_3Phen]$ in toluene (λ_{ex} = 350 nm).[42]

Reagents and Antibodies

P19C and **P19** were synthesized in GL Biochem (Shanghai) Ltd. The LMP1 antibody was purchased from Abcam. The antibodies including anti-LMP1 were purchased from kerafast, while anti-NF-κB p65, anti-NF-κB p105/50, antihistone H3, and anti-GAPDH were purchased from Cell Signaling Technology. Antirabbit IgG HRP-linked, antimouse IgG HRP-linked, and protease/phosphatase inhibitor cocktail were purchased from Cell Signaling Technology. Alexa Fluor 488-conjugated goat antimouse IgG, NucBlue fixed cell ready probes (DAPI), and ProLong gold antifade mountant with DAPI were purchased from Invitrogen. The transcriptional response element (TRE)-fluorescent protein reporter, pTRE-EGFP plasmid, was constructed as previously reported.[43]

Cell Line and Culture

LCL3, AG876, AFB1, and C666-1 cells were grown in an RPMI-1640 medium. HeLa cells were cultivated in a DMEM medium, and MRC5 cells were cultivated in an MEM medium (Gibco, U.S.A.). All media are supplemented with 10% fetal bovine serum and 1% penicillin/streptomycin antibiotics. All the cells are cultivated in a humidified incubator with 5% CO_2 at 37 °C. The pTRE-EGFP plasmid was transduced into LCL3 cells as previously mentioned.[44]

Western Blot Analysis

Cells with different treatments were harvested and washed with phosphate-buffered saline (PBS). Lysis buffer supplied by 1X proteases-phosphatase inhibitor were added into the cells for 5 min on ice. Then the samples were centrifuged at 14 000 × *g* at 4 °C for 20 min. The fractionated cell lysates were subjected to SDS-PAGE gel and transferred onto PVDF membranes. Membranes were then blocked by 3% nonfat milk for 30 min at room temperature and incubated with specific primary antibodies at 4 °C overnight. They were then washed with TBST buffer and incubated with the corresponding secondary antibodies for 1 h at room temperature. Then, the membranes were washed with TBST, and the chemiluminescence substrate was added onto the membrane surface. The ChemiDoc XRS system and Image Lab Software were used to visualize the blot.

Immunoluminescence Assay

These assays were prepared and conducted at room temperature, unless otherwise stated. Cells with different treatments were fixed by formalin for 15 min. The samples were then washed with PBS, and 0.2% Triton-X buffer was added onto the samples for 15 min. The 3% BSA in PBS served as the blocking buffer and was applied onto the sample for 30 min at room temperature. The primary antibody was diluted in blocking buffer and added onto the sample at 4 °C overnight. The samples were washed with PBS, and the corresponding secondary antibodies were added over 1 h. Samples were washed with PBS, and mountant was applied to each sample. Images were acquired either using a 370 nm laser excitation or from a 370 nm LED excitation of a Nikon Eclipse Ti2 Confocal Microscope. NIR images were captured by a NIRvana TE 640 camera. The signal enhancement of the C666-1 images was obtained by enhancing the exposure of the captured images by the NIS element AR software. Multiphoton microscopy was conducted by the Leica TCS SP8MP System.

In Vivo Inhibition Assays

LCL3 cells were suspended at 1 × 10^7 in 200 μL of serum-free medium (RPMI 1640) and then injected into the right flank of female six- to eight-week-old NSG mice. When the tumors reached an average volume of approximately 400 mm^3, intratumor injections were performed twice a week. Tumor bearing mice were randomly divided into three groups, three mice in a group. **EuP19** and **P19C** in PBS buffer at the desired dose (25 μg/injection) was injected directly into the tumor. PBS buffer served as the control. All the injections were performed in 100 μL/injection. Body weight and tumor volumes were measured twice per week. Tumor volumes were calculated on the basis of the equation volume $V = (L \times W^2)/2$, where L and W refer to the longer and shorter dimensions, respectively. After a 16-day treatment, the mice were sacrificed, and their tumors were collected and weighed. Investigators were blind to the treatment groups during the experiments and data analysis. All animal experiments were approved by the Department of Health of the Hong Kong Government and the Hong Kong Baptist University Committee on the Use of Human and Animal Subjects in Teaching and Research.

Computational Details

The *N*-terminal region of the LMP1 protein was modeled using the I-TASSER online server (Iterative Threading Assembly Refinement).[45] It was constructed based on the structure of the membrane domain of respiratory protein of *E. coli* (PDB ID: 3RKO), the ovine respiratory complex (PDB ID: 5LNK), the sweet transporter (PDB ID: 5CTG), and NE. Coli YajR transporter (PDB ID: 3WDO). The modeled structure was then checked and matched with the experimentally defined TM region of the LMP1 protein at the *N*-terminus. **P19** and **P19C** were docked into the modeled *N*-terminal of LMP1 protein using CABS-dock.[46] The most probable docked conformations of **P19** and **P19C** were selected and used for further analysis.

■ ASSOCIATED CONTENT

Supporting Information

The Supporting Information is available free of charge at https://pubs.acs.org/doi/10.1021/jacsau.1c00187.

Synthetic procedures, additional photophysical characterization of compounds, and complementary data (NMR, HPLC, MALDI-TOF HRMS) (PDF)

■ AUTHOR INFORMATION

Corresponding Authors

Ka-Leung Wong − *Department of Chemistry, Hong Kong Baptist University, Hong Kong SAR, China;* orcid.org/0000-0002-3750-5980; Email: klwong@hkbu.edu.hk

Hong Lok Lung − *Department of Chemistry, Hong Kong Baptist University, Hong Kong SAR, China;* Email: hllung2@hkbu.edu.hk

Lijun Jiang − *Department of Applied Biological and Chemical Technology, Hong Kong Polytechnic University, Hong Kong SAR, China;* Email: lijun.jiang@polyu.edu.hk

Jean-Claude G. Bünzli − *Department of Chemistry, Hong Kong Baptist University, Hong Kong SAR, China; ISIC, Swiss Federal Institute of Technology (EPFL), CH-1015 Lausanne, Switzerland;* Email: jean-claude.bunzli@epfl.ch

Nicholas J. Long − *Department of Chemistry, Imperial College London, London W12 0BZ, United Kingdom;* orcid.org/0000-0002-8298-938X; Email: n.long@imperial.ac.uk

https://doi.org/10.1021/jacsau.1c00187
JACS Au 2021, 1, 1034−1043

Authors

Ho-Fai Chau − *Department of Chemistry, Hong Kong Baptist University, Hong Kong SAR, China*

Yue Wu − *Department of Chemistry, Hong Kong Baptist University, Hong Kong SAR, China*

Wan-Yiu Fok − *Department of Chemistry, Hong Kong Baptist University, Hong Kong SAR, China*

Waygen Thor − *Department of Chemistry, Hong Kong Baptist University, Hong Kong SAR, China;* orcid.org/0000-0002-4366-9113

William Chi-Shing Cho − *Department of Clinical Oncology, Queen Elizabeth Hospital, Kowloon, Hong Kong SAR, China;* orcid.org/0000-0003-4174-4586

Ping'an Ma − *State Key Laboratory of Rare Earth Resource Utilization, Changchun Institute of Applied Chemistry, Chinese Academy of Sciences, Changchun 130022, China*

Jun Lin − *State Key Laboratory of Rare Earth Resource Utilization, Changchun Institute of Applied Chemistry, Chinese Academy of Sciences, Changchun 130022, China;* orcid.org/0000-0001-9572-2134

Nai-Ki Mak − *Department of Biology, Hong Kong Baptist University, Hong Kong SAR, China*

Complete contact information is available at: https://pubs.acs.org/10.1021/jacsau.1c00187

Author Contributions

The manuscript was written through contributions of all authors.

Notes

The authors declare no competing financial interest.

■ ACKNOWLEDGMENTS

This work was supported by grants from Hong Kong Research Grant Council (HKBU 12300117), the CAS-Croucher Funding Scheme for Joint Laboratories (CAS18204), the Hong Kong Research Grants Council Collaborative Research Fund Scheme (C4001-18GF), BP, Tsinghua, HKBU Joint Lab for EBV associated Cancer and Health and Medical Research Fund (18170022). and Hong Kong Baptist University RC-ICRS/17-18/01. J.-C.G.B. thanks HKBU for the Dr. Kennedy Wong Distinguished Visiting Professorship (2017−2019). N.J.L. thanks HKBU for the Dr. Kennedy Wong Distinguished Visiting Professorship (2021−2023). K.-L.W. would like to thank the support from the Dr. Mok Man Hung Endowed Professorship in HKBU Chemistry.

■ REFERENCES

(1) Macsween, K. F.; Crawford, D. H. Epstein-Barr virus-recent advances. *Lancet Infect. Dis.* **2003**, *3*, 131−140.

(2) Jiang, L.; Xie, C.; Lung, H. L.; Lo, K. W.; Law, G.-L.; Mak, N.-K.; Wong, K.-L. EBNA1-targeted inhibitors: Novel approaches for the treatment of Epstein-Barr virus-associated cancers. *Theranostics* **2018**, *8*, 5307−5319.

(3) Young, L. S.; Rickinson, A. B. Epstein-Barr virus: 40 years on. *Nat. Rev. Cancer* **2004**, *4*, 757−768.

(4) Dawson, C. W.; Port, R. J.; Young, L. S. The role of the EBV-encoded latent membrane proteins LMP1 and LMP1 in the pathogenesis of nasopharyngeal carcinoma (NPC). *Semin. Cancer Biol.* **2012**, *22*, 144−153.

(5) Young, L. S.; Murray, P. G. Epstein-Barr virus and oncogenesis: from latent genes to tumors. *Oncogene* **2003**, *22*, 5108−5121.

(6) Kaye, K. M.; Izumi, K. M.; Kieff, E. Epstein-Barr virus latent membrane protein 1 is essential for B-lymphocyte growth transformation. *Proc. Natl. Acad. Sci. U. S. A.* **1993**, *90* (19), 9150−9154.

(7) Wang, D.; Liebowitz, D.; Kieff, E. An EBV membrane protein expressed in immortalized lymphocytes transforms established rodent cells. *Cell* **1985**, *43*, 831−840.

(8) Kilger, E.; Kieser, A.; Baumann, M.; Hammerschmidt, W. Epstein-Barr virus-mediated B-cell proliferation is dependent upon latent membrane protein 1, which stimulates an activated CD40 receptor. *EMBO J.* **1998**, *17*, 1700−1709.

(9) Zheng, H.; Li, L. L.; Hu, D. S.; Deng, X. Y.; Cao, Y. Role of Epstein-Barr virus encoded latent membrane protein 1 in the carcinogenesis of nasopharyngeal carcinoma. *Cell Mol. Immunol.* **2007**, *4*, 185−196.

(10) Morris, M. A.; Dawson, C. W.; Young, L. S. Role of the Epstein-Barr virus-encoded latent membrane protein-1, LMP1, in the pathogenesis of nasopharyngeal carcinoma. *Future Oncol.* **2009**, *5*, 811−825.

(11) Raab-Traub, N. Novel mechanisms of EBV-induced oncogenesis. *Curr. Opin. Virol.* **2012**, *2*, 453−458.

(12) Soni, V.; Cahir-McFarland, E.; Kieff, E. LMP1 TRAFficking activates growth and survival pathways. *Adv. Exp. Med. Biol.* **2007**, *597*, 173−187.

(13) Raab-Traub, N. Epstein-Barr virus transforming proteins: Biologic properties and contribution to oncogenesis. In *DNA Tumor Viruses*; Damania, B., Pipas, J. M., Eds.; Springer: New York, NY, U.S.A., 2009; Vol. *1*, pp 259−284.

(14) Dawson, C. W.; Tramountanis, G.; Eliopoulos, A. G.; Young, L. S. Epstein-Barr virus latent membrane protein 1 (LMP1) activates the phosphatidylinositol 3-kinase/Akt pathway to promote cell survival and induce actin filament remodeling. *J. Biol. Chem.* **2003**, *278*, 3694−3704.

(15) Ersing, I.; Bernhardt, K.; Gewurz, B. E. NF- B and IRF7 pathway activation by Epstein-Barr virus latent membrane protein 1. *Viruses* **2013**, *5* (6), 1587−1606.

(16) Lee, D. Y.; Sugden, B. The latent membrane protein 1 oncogene modifies B-cell physiology by regulating autophagy. *Oncogene* **2008**, *27*, 2833−42.

(17) Coffin, W. F., III; Geiger, T. R.; Martin, J. M. Transmembrnae domains 1 and 2 of the latent membrane protein 1 of Epstein-Barr virus contain a lipid raft targeting signal and play a critical role in cytostasis. *J. Virol.* **2003**, *77* (6), 3749−3758.

(18) Kaykas, A.; Worringer, K.; Sugden, B. CD40 and LMP-1 both signal from lipid rafts but LMP-1 assembles a distinct, more efficient signalling complex. *EMBO J.* **2001**, *20* (11), 2641−2654.

(19) Yasui, T.; Luftig, M.; Soni, V.; Kieff, E. Latent infection membrane protein transmembrane FWLY is critical or intermolecular interation, raft localization, and signalling. *Proc. Natl. Acad. Sci. U. S. A.* **2004**, *101*, 278−283.

(20) Kaykas, A.; Worringer, K.; Sugden, B. LMP-1's transmembrane domains encode multiple functions required for LMP-1's efficient signalling. *J. Virol.* **2002**, *76*, 11551−11560.

(21) Soni, V.; Yasui, T.; Cahir-McFarland, E.; Kieff, E. LMP1 transmembrane domain 1 and 2 (TM1−2) FWLY mediates intermolecular interactions with TM3−6 to activate NK-kappaB. *J. Virol.* **2006**, *80*, 10787−10793.

(22) Cieslikiewicz-Bouet, M.; Eliseeva, S. V.; Aucagne, V.; Delmas, A. F.; Gillaizeau, I.; Petoud, S. Near-infrared emitting lanthanide(iii) complexes as prototypes of optical imaging agents with peptide targeting ability: a methodological approach. *RSC Adv.* **2019**, *9*, 1747−1751.

(23) Chan, C.-F.; Lan, R.; Tsang, M. K.; Zhou, D.; Lear, S.; Chan, W.-L.; Cobb, S. L.; Wong, W.-K.; Hao, J.; Wong, W.-T.; Wong, K.-L. Directional Plk1 inhibition-driven cell cycle interruption using amphiphilic thin-coated peptide-lanthanide upconversion nanomaterials as in vivo tumor suppressors. *J. Mater. Chem. B* **2015**, *3*, 2624−2634.

(24) Yan, J.; He, W.; Yan, S.; Niu, F.; Liu, T.; Ma, B.; Shao, Y.; Yan, Y.; Yang, G.; Lu, W.; Du, Y.; Lei, B.; Ma, P. X. Self-Assembled

Peptide−Lanthanide Nanoclusters for Safe Tumor Therapy: Overcoming and Utilizing Biological Barriers to Peptide Drug Delivery. *ACS Nano* **2018**, *12* (2), 2017−2026.
(25) He, W.; Yan, J.; Wang, L.; Lei, B.; Hou, P.; Lu, W.; Ma, P. X. A lanthanide-peptide-derived bacterium-like nanotheranostic with high tumor-targeting, -imaging and -killing properties. *Biomaterials* **2019**, *206*, 13−24.
(26) Liang, L.; Astruc, D. The Copper(I)-Catalyzed Alkyne-Azide Cycloaddition (CuAAC) "Click" Reaction and Its Applications. *Coord. Chem. Rev.* **2011**, *255* (23−24), 2933−2945.
(27) Cobb, S. L.; Chan, C.-F.; Law, G.-L.; Lee, C.-S.; Li, H.; Chadbourne, F. L.; Chan, W.-L.; Lan, R.; Wong, K.-L. Real Time Detection of Cell Cycle Regulator Cyclin A on Living Tumor Cells with Europium Emission. *Dalt. Trans.* **2013**, *42* (37), 13495.
(28) Li, H.; Xie, C.; Lan, R.; Zha, S.; Chan, C. F.; Wong, W. Y.; Ho, K. L.; Chan, B. D.; Luo, Y.; Zhang, J. X.; et al. A Smart Europium-Ruthenium Complex as Anticancer Prodrug: Controllable Drug Release and Real-Time Monitoring under Different Light Excitations. *J. Med. Chem.* **2017**, *60* (21), 8923−8932.
(29) Liang, Z.; Chan, C. F.; Liu, Y.; Wong, W. T.; Lee, C. S.; Law, G. L.; Wong, K. L. The Effects of the Increasing Number of the Same Chromophore on Photosensitization of Water-Soluble Cyclen-Based Europium Complexes with Potential for Biological Applications. *RSC Adv.* **2015**, *5* (18), 13347−13356.
(30) Li, H.; Lan, R.; Chan, C. F.; Jiang, L.; Dai, L.; Kwong, D. W. J.; Lam, M. H. W.; Wong, K. L. Real-Time in Situ Monitoring via Europium Emission of the Photo-Release of Antitumor Cisplatin from a Eu-Pt Complex. *Chem. Commun.* **2015**, *51* (74), 14022−14025.
(31) Bolte, S.; Cordelières, F. P. A guided tour into subcellular colocalization analysis in light microscopy. *J. Microsc.* **2006**, *224*, 213−232.
(32) Giridharan, S.; Srinivasan, M. Mechanisms of NF-κB p65 and strategies for therapeutic manipulation. *J. Inflammation Res.* **2018**, *11*, 407−419.
(33) Li, Y. Y.; Chung, G. T. Y.; Lui, V. W. Y.; To, K.; Ma, B. B. Y.; Chow, C.; Woo, J. K. S.; Yip, K. Y.; Seo, J.; Hui, E. P.; Mak, M. K. F.; Rusan, M.; Chau, N. G.; Or, Y. Y. Y.; Law, M. H. N.; Law, P. P. Y.; Liu, Z. W. Y.; Ngan, H.; Hau, P.; Verhoeft, K. R.; Poon, P. H. Y.; Yoo, S.; Shin, J.; Lee, S.; Lun, S. W. M.; Jia, L.; Chan, A. W. H.; Chan, J. Y. K.; Lai, P. B. S.; Fung, C.; Hung, S.; Wang, L.; Chang, A. M. V.; Chiosea, S. I.; Hedberg, M. L.; Tsao, S.; van Hasselt, A. C.; Chan, A. T. C.; Grandis, J. R.; Hammerman, P. S.; Lo, K. Exome and genome sequencing of nasopharynx cancer identifies NF-κB pathway activating mutations. *Nat. Commun.* **2017**, *8*, 14121.
(34) Benders, A. A.; Tang, W.; Middeldorp, J. M.; Greijer, A. E.; Thorne, L. B.; Funkhouser, W. K.; Kimryn Rathmell, W.; Gulley, M. L. Epstein-Barr virus latent membrane protein 1 is not associated with vessel density nor with hypoxia inducible factor 1 alpha expression in nasopharyngeal carcinoma tissue. *Head Neck Pathol.* **2009**, *3* (4), 276−282.
(35) Chen, Y. P.; Chan, A. T. C.; Le, Q.; Blanchard, P.; Sun, Y.; Ma, J. Nasopharyngeal carcinoma. *Lancet* **2019**, *394* (10192), 64−80.
(36) Lo, A. K.; To, K. F.; Lo, K. W.; Lung, R. W. M.; Hui, J. W. Y.; Liao, G.; Hayward, S. D. Modulation of LMP1 protein expression by EBV-encoded microRNAs. *Proc. Natl. Acad. Sci. U. S. A.* **2007**, *104* (41), 16164−16169.
(37) Hu, L. F.; Chen, F.; Zhen, Q. F.; Zhang, Y. W.; Luo, Y.; Zheng, X.; Winberg, G.; Ernberg, I.; Klein, G. Differences in the growth pattern and clinical course of EBV-LMP1 expressing and non-expressing nasopharyngeal carcinomas. *Eur. J. Cancer* **1995**, *31a* (5), 658−660.
(38) Horikawa, T. T.; Yoshizaki, T.; Sheen, T.; Lee, S.; Furukawa, M. Association of latent membrane protein 1 and matrix metalloproteinase 9 with metastasis in nasopharyngeal carcinoma. *Cancer* **2000**, *89* (4), 715−723.
(39) Horikawa, T. T.; Sheen, T. S.; Takeshita, H.; Sato, H.; Furukawa, M.; Yoshizaki, T. Induction of c-Met proto-oncogene by Epstein-Barr virus latent membrane protein-1 and the correlation with cervical lymph node metastasis of nasopharyngeal carcinoma. *Am. J. Pathol.* **2001**, *159* (1), 27−33.
(40) Chen, J.; Hu, C.; Hou, J.; Shao, Q.; Yan, Li; Zhu, X.; Zeng, Y.; Shao, J. Epstein-Barr virus encoded latent membrane protein 1 regulates mTOR signaling pathway genes which predict poor prognosis of nasopharyngeal carcinoma. *J. Transl. Med.* **2010**, *8*, 30.
(41) Chen, Y. P.; Zhang, W.; Chen, L.; Tang, L.; Mao, Y.; Li, W.; Liu, X.; Zhou, G.; Sun, Y.; Kang, T.; Zeng, M.; Liu, N.; Ma, J. Effect of latent membrane protein 1 expression on overall survival in Epstein-Barr virus-associated cancers: a literature-based meta-analysis. *Oncotarget* **2015**, *6* (30), 29311−29323.
(42) Tsvirko, M. P.; Meshkova, S. B.; Venchikov, V. Y.; Topilova, Z. M.; Bol'shoi, D. V. Determination of contributions of various molecular groups to nonradiative deactivation of electronic excitation energy in β-diketonate complexes of ytterbium(III). *Opt. Spectrosc.* **2001**, *90*, 669−673.
(43) e Silva, F.R.G. e; Menezes, J. F. S.; Rocha, G. B.; Alves, S.; Brito, H. F.; Longo, R. L.; Malta, O. L. Emission quantum yield of europium (III) mixed complexes with thenoyltrifluoroacetonate and some aromatic ligands. *J. Alloys Compd.* **2000**, *303−304*, 364−370.
(44) Shuen, W. H.; Kan, R.; Yu, Z.; Lung, H. L.; Lung, M. L. Novel lentiviral-inducible transgene expression systems and versatile single-plasmid reporters for *in vitro* and *in vivo* cancer biology studies. *Cancer Gene Ther.* **2015**, *22* (4), 207−214.
(45) Yang, J.; Yan, R.; Roy, A.; Xu, D.; Poisson, J.; Zhang, Y. The I-TASSER Suite: Protein structure and function prediction. *Nat. Methods* **2015**, *12*, 7−8.
(46) Kurcinski, M.; Jamroz, M.; Blaszczyk, M.; Kolinski, A.; Kmiecik, S. CABS-dock web server for the flexible docking of peptides to proteins without prior knowledge of the binding site. *Nucleic Acids Res.* **2015**, *43* (W1), W419−W424.

https://doi.org/10.1021/jacsau.1c00187
JACS Au 2021, 1, 1034−1043